Wavelet analysis of the extreme wave load test of a flexible ship model

S.X. Du, D. Hudson, W.G. Price and P. Temarel

University of Southampton, Ship Science,

Southampton, SO17 1BJ, UK

R.Z Chen, Y.S. Wu

China Ship Scientific Research Center, Wuxi, Jiangsu, 214082, China

Abstract

This study describes an application of a Daubechies wavelet function to analyze measured ship model data. The records of a self-propelled, flexible model of the S175 container ship moving in waves are analyzed by FFT and wavelet methods. It is shown that the high frequency component of the recorded rigid body motions can be omitted without substantially affecting the main features of the data set relating to dynamic loads. The decomposition of the bending moment time history into low and high frequency components allows the time of impact occurrence and its amplitude to be easily detected. Such quantities provide important information for the development of generic and realistic transient impact (e.g. slamming, green water) force models for ships travelling in waves.

1 Introduction

A ship in unrestricted service inevitably encounters severe sea states even when current improvements in weather routing systems are taken into account (ISSC VI.1, 2000). Non-linear effects on wave-induced loads, motions and structural responses are often significant for a ship travelling in moderate and severe waves. The slamming and green water impact loads are impulsive loads on local and global structures, inducing transient, high level, stresses on ship structures. Springing and whipping responses of ocean going vessels are usually observed in moderate and severe sea states. They are low damping vibratory phenomena of the hull girder near the 2-node natural frequency of the global ship hull vibration and implied basically continuous and possibly caused by stem slamming in the moderate sea states (Storhaug et al, 2003). However, in the sagging condition higher peaks were detected following whipping response, which are determined directly by non-linear effects associated with transient bow flare slamming loads (Cusano et. al, 2003; Chen et al, 2001). The green water problem is an extreme nonlinear wave-structure interaction occurring in rough sea states or by freak waves. Large value, impulsive green water impact loads are considered the cause of damage to ship structures, especially superstructure and ship equipment in the bow region (Stansberg and Karlsen, 2001; Faltinsen et al, 2002).

Full-scale measurements and model test investigations of slamming effects and green water impact on ship structures allow the determination of design loads and the verification of prediction methods of loads and responses. In a holistic analysis of ship structures it is important to identify the different types of hydrodynamic loads contributing to the total bending moment, (i.e., ordinary wave loads and slamming force) in terms of magnitude, phase lag relative to the wave-induced peak and decay rate (Jensen and Mansour, 2003). The benefit of characterizing these contributions lies in estimation of their relative importance with respect to different vessel operational conditions. This allows predictions of possible dangerous situations and to design, if necessary, structural modifications able to reduce global ship elastic responses (Ciappi et al, 2003).

Plastic materials enable an entirely elastic ship model to be manufactured allowing for reasonable satisfaction of the similitude principle. In contrast to using a segmented model, the elastic model provides the means of measuring detailed structural response information over the whole hull of the ship, including bending moment, shearing force, torque at any cross section, etc. (Wu et al, 2003). The purpose of the S175 flexible model ship tests carried out in CSSRC is to study wave-induced loads and motion responses of the ship in severe waves, focusing on the non-linearity of the loads with respect to waveheight (Chen et al, 2001). The wavelet analysis in the present study is based on data measured in these tests.

Wavelets are a relatively new mathematical tool to analyze time series data, but in many respects, wavelets are a synthesis of older ideas producing new elegant mathematical results and efficient computational algorithms (Percival and Walden, 2000). In particular, a wavelet analysis, presents time and frequency localization of measured data, and is a suitable numerical tool to approximate data with sharp discontinuities or sharp

variations. An interesting application of wavelets was presented by Newland (1993) to analyze the vibration records of a two-degree-of-freedom system, in which one response is a stationary random process to white noise excitation and the other a non-stationary response to an impulsive excitation. Patsias et al (2002 a, b) used image sequences and wavelets to extract natural frequencies, modal damping and mode shapes in a structural dynamics study. Kwon et al (2001) analyzed the ringing phenomenon of a vertical circular cylinder in breaking waves by using continuous Morlet wavelet transforms (Percival and Walden, 2000). They showed that high frequency components (ringing) were generated at the onset of the breaking wave impact in the time domain, which is hardly detectable if one relies on traditional spectral analysis.

In this paper, a brief description of a wavelet analysis procedure is presented adopting Daubechies wavelet functions (Daubechies, 1992). The measured data of a self-propelled, flexible model of the S175 container ship travelling in severe regular waves is analyzed by a Fourier analysis method and the proposed wavelet method. Non-linear heave and pitch motions, vertical accelerations, vertical bending moment data on several transverse sections of the ship are presented using the different methods. The numerical results show that Daubechies wavelet function series reconstructs the measured data in the time domain precisely, and decomposes time history records at several different frequency levels. By using a filtering technique in the wavelet analysis, it is demonstrated that the high frequency component of the recorded rigid body motion signals can be omitted without substantially affecting the main features of the data set. This high frequency content is induced by local flexible responses arising at the point of installation of the measuring devices. By decomposing the vertical bending moment time history into low frequency and high frequency components, impact occurrence is easily detected, and impact characteristics (i.e. maximum value, duration, decay behaviour, etc) exhibited by the fluid-structure interaction system and transient force determined. This information can be used in the generation of empirical formulae to describe transient impact forces acting on ships travelling in severe waves.

2 Basic formulas in wavelet analysis

In contract to Unlike Fourier transform techniques utilizing only orthogonal sine and cosine functions, wavelet transforms have an infinite set of possible basis functions, (for example, Harr's simple wavelets and Daubechies wavelets, etc), as discussed by Nievergelt (1999). This provides choice when analyzing signals. In addition, sine and cosine functions extend over the whole time period, whereas wavelet functions grow and decay in limited time periods. This unique property allows the wavelet method to identity time and frequency localizations of signals. A compactly supported wavelet family consists of a scaling function $\varphi(x)$ with vanishing moment number N satisfy the conditions

$$\begin{aligned} &\varphi(x) = 0, \ \text{for} \ x < M_1 \ \text{or} \ x > M_2, (M_1 < M_2 \in I), \\ &\int_{\Re} x^N \varphi(x) dx = 0, \\ &\int_{\Re} \varphi(2x-k)\varphi(2x-j)dx = 0, \ \text{for} \ k \neq j \ \text{and} \ j,k \in I. \end{aligned} \tag{1}$$

where M_1 and M_2 are integer constants.

The family of Daubechies wavelets (Daubechies, 1992) is used in the present study. The scaling function (or father function, basic building block) $\varphi(x)$ for $x<M_1=0$ or $x>M_2=2N-1$ is determined by the recursive relation

$$\varphi(x) = \sum_{k=0}^{2N-1} h_k \varphi(2x-k). \tag{2}$$

N denotes the vanishing moment number defined in equation (1).

In this two-scale dilation equation, the value of the scaling function $\varphi(x)$ is evaluated by the weighted sum of the Daubechies scaling filters h_k, if the initial values of $\varphi(x)$ at integer points are known, where $x \in D_n \{m \cdot 2^{-n}\}$, $m,n \in I$ for all dyadic numbers. The wavelet function (or mother function) is estimated by the weighted sum of the wavelet filters g_k, which is a function composed of the conjugate of h_{1-k}, denoted by $\overline{h_{1-k}}$, if the initial values of $\varphi(x)$ at integer points are known. That is,

$$\begin{aligned} &\psi(x) = \sum_{k=2-2N}^{1} g_k \varphi(2x-k), \\ &g_k = (-1)^k \overline{h_{1-k}}. \end{aligned} \tag{3}$$

The filters h_k satisfy the general relation,

$$\sum_{k=0}^{N-1} h_{2k} = 1 = \sum_{k=0}^{N-1} h_{2k+1}, \tag{4}$$

and their values for the Daubechies wavelets family are usually determined by a spectral factorization method (Daubechies, 1992).

Once the filter coefficients are known, the initial values of $\varphi(x)$ at integer points can be calculated by solving the following eigenvalue equations,

$$\begin{bmatrix} h_1 & h_0 & & \\ h_3 & h_2 & h_1 & h_0 \\ & \cdots & & \\ h_{2N-1} & h_{2N-2} & & \end{bmatrix} \begin{bmatrix} \varphi(1) \\ \varphi(2) \\ \cdots \\ \varphi(2N-2) \end{bmatrix} = \begin{bmatrix} \varphi(1) \\ \varphi(2) \\ \cdots \\ \varphi(2N-2) \end{bmatrix} \tag{5}$$

which arises from the recursive relation described in equation (2).

The eigenvector, which corresponds to the eigenvalue of 1, is the set of the initial values of $\varphi(x)$ normalized by the form

$$\sum_{k=1}^{2N-2} \varphi(k) = 1, \tag{6}$$

together with $\varphi(0) = 0, \varphi(2N-1) = 0$. The values of scaling function $\varphi(x)$ and wavelet function $\psi(x)$ at any dyadic number $x \in D_n \equiv \{m \cdot 2^{-n}\}$, $m,n \in I$ are determined from equations (2) and (3). Figure 1 illustrates examples of the forms of Daubechies wavelet bases for different N values.

Similar to a discrete Fourier transform method, the discrete wavelet transform requires an extension of the data series $S_0, S_1, \ldots, S_{2^n-1}$ with a constant interval step into a periodic data set of 2^{n+1} entries, i.e. $S_0, S_1, \ldots, S_{2^n-1}, S_{2^n}, \ldots, S_{2^{n+1}-1}$. To require small edge effect due to this extension, a mirror extension or cubic spline extension method is usually adopted (Nievergelt, 1999). In this study, a mirror extension method is adopted with symmetry slopes at the ends of data imposed. The extended samples are determined from the relations

$$\begin{aligned} S_{2^n+j} &= S_{2^n-1-j}, \quad \forall\, 0 < j < 2^n - 1, \\ S_{2^n} &= 2S_{2^n-1} - S_{2^n-2}, \\ S_{2^{n+1}-1} &= 2S_0 - S_1. \end{aligned} \tag{7}$$

Once the family of wavelets is chosen and the data series $S_0, S_1, \ldots, S_{2^n-1}$, of constant interval step, extended into a periodic data set of 2^{n+1}, the signals can be expressed approximately by the scaling function

$$\begin{aligned} \tilde{f}(x) &= \sum_{j=0}^{2^{n+1}-1} a_j \varphi(x - j), \\ a_j &= \sum_{i=0}^{2N-1} \varphi(i) S_{j+i}. \end{aligned} \tag{8}$$

Due to the periodic property of the extended signal series, the series of coefficients $a_0, a_1, \ldots, a_{2^{n+1}-1}$ are also a periodic data set. Substituting equations (2) and (3) into equation (8), we find that the signal expression is replaced by an equivalent combination of 2^n lower frequency level scaling functions $\varphi(\frac{x}{2} - j)$ and 2^n lower frequency level wavelet functions $\psi(\frac{x}{2} - j)$, of the form

$$\begin{aligned} \tilde{f}(x) = &\sum_{j=0}^{2^n-1} a_j^{(n-1)} \varphi(\frac{x}{2} - j) \\ &+ \sum_{j=0}^{2^n-1} c_j^{(n-1)} \psi(\frac{x}{2} - N + 1 - j), \end{aligned} \tag{9}$$

where

$$a_j^{(0)} = a_j,$$
$$a_j^{(n-1)} = \frac{1}{2}\sum_{i=0}^{2N-1} h_i a_{j+i}^{(n)},$$
$$c_j^{(n-1)} = \frac{1}{2}\sum_{i=2-2N}^{1} g_i a_{j+i}^{(n)}.$$

The coefficient $a_j^{(n-1)}$ measures the weighted average of the function $\tilde{f}(x)$ near the 'jth ' point of the data set on frequency level (n-1), and $c_j^{(n-1)}$ measures the weighted change in the function near the 'jth' point.

Repetition of this procedure for the term including $a_j^{(n-m)}, m = 1,..,n$ and accounting for the periodic behaviour of the extended series of samples, the signal expression takes the form

$$\begin{aligned}\tilde{f}(x) = {} & a_0^{(-1)}\sum_{j=0}^{2N-1}\varphi\left(\frac{x}{2^{n+1}} - j\right) \\ & + c_0^{(-1)}\sum_{j=0}^{2N-1}\psi\left(\frac{x}{2^{n+1}} - N + 1 - j\right) \\ & + \sum_{m=1}^{n}\sum_{j=0}^{2^{n-m+1}-1} c_j^{(n-m)}\psi\left(\frac{x}{2^m} - N + 1 - j\right)\end{aligned} \tag{10}$$

where

$$a_j^{(n-m)} = \frac{1}{2}\sum_{i=0}^{2N-1} h_i a_{j+i}^{(n-m+1)},$$
$$c_j^{(n-m)} = \frac{1}{2}\sum_{i=2-2N}^{1} g_i a_{j+i}^{(n-m+1)}.$$

Equation (10) represents a linear operation and provides the wavelet expression describing a series of data by a series of functions originally arising from basis scaling functions and wavelet functions by shifting and compressing the independent variable x. At each frequency level (n-m) (m=1, 2, …, n+1), the basis functions are localized both in frequency (by compression in the form of $\frac{x}{2^m}$) and in space (or time) (by shifting a distance of N-1+j).

Wavelet decomposition is a similar process to a windowed Fourier transform, in the sense that the window is simply a wave base that is compactly supported within $(\frac{x}{2^m} - N + 1 - j) \in [-N+1, N]$. However, an advantage of wavelet transforms over a windowed Fourier transform is that the size of *windows* vary between different frequency levels (Daubechies, 1992). From equation (10), we can see that changes in the function $\tilde{f}(x)$ at each frequency level are determined by the values of $c_j^{(n-m)}(m = 1,2,...,n+1)$. A larger value of $c_j^{(n-m)}$ at a higher level (n-m) implies signal discontinuities or transient oscillations at the location.

3 Extreme wave load tests on a flexible ship model

In general, an elastic ship model satisfies the geometric similarity of the hull form, hydrodynamic similarity, together with structural similarity with regard to the global vertical bending and shearing, and hence may be used to predict hull girder wave loads, motions and global structural responses (Wu et al, 2003). As discussed by Lin et al.(1991), ideally the material chosen for this kind of model is characterized by the following properties:

(a). The Young's modulus of the material is less than that of steel by an order of 10^{-2} and its Poisson ratio value close to that of steel.

(b). The material is isotropic with a comparatively large region of linear strain-stress relationship.

(c). Within the linear region, the material exhibits stable mechanical properties and no distinguishable creepage in normal conditions at atmospheric temperature.

(d). The construction of the model (i.e. formalizing and adhering) is easily performed.

As shown in Table 1, the mechanical properties of ABS702 material conforms closely to these requirements. For this reason, two flexible models were made of this material and tested in the wave basin of CSSRC (Lin et. al., 1991; Li, et. al, 1996). The same material was used for the present self-propelled flexible model of the S175 container ship.

Chen et al (2001) described in detail the flexible model manufacturing process. The principal particulars of the S175 flexible model are shown in Table 2. The thickness of the plastic plates for the hull is 2mm, and 4mm for bulkhead, keel and girder located on the deck. In total 21 transverse bulkheads at each station from 0 to 20 were used to reinforce the transverse stiffness of the model and to locate ballast blocks. The weight and locations of the ballast blocks were suitably arranged to satisfy the similitude of the weight distribution along the length and the location of the centre of gravity of the ship.

Table 1 Mechanical properties of ABS702

Item	Value	Temperature condition
Young's Modulus	2.84×10^9 N/m^2	8^o-29^o C
Poisson ratio	0.343	8^o-29^o C
Density	1.09 g/cm^3	
Rate of water absorption	1.69%	25^o C
$\lvert E_{mx} - E_{my} \rvert / E_{mx}$	< 2.61%	8^o-29^o C
Linear region	ε<2000$\mu\varepsilon$	

Table 2 Principal particulars of the S175 Container ship

Items	Prototype	Model
L_{pp} (Length between perpendiculars, m)	175.00	3.6
B (Beam, m)	25.40	0.523
D (Depth, m)	15.40	0.317
T (Draught, m)	9.50	0.195
Δ (Displacement mass)	24742t	215.25kg
K_{yy} (Radius of longitudinal gyration)	$0.236L_{pp}$	$0.236L_{pp}$
FG (Longitudinal center of gravity from forward perpendicular, m)	90.0	1.851
GM (Metacenter height, m)	1.0	0.021
KM (Transverse metacenter above keel, m)	10.52	0.216
EI (Bending rigidity at midship, kg·mm^2)	2.28×10^{18}	10.66×10^9
f (2-node frequency, Hz)	1.60	12.57

The model was self-propelled able to travel with the carriage. It was allowed to freely surge, heave, pitch and vibrate vertically. Sway, roll and yaw motions were restricted. The speed of the model was set for a prescribed propeller revolution rate of the ship and was measured by the speed of the towing carriage.

Stresses and vertical bending moments were recorded at selected positions along the model, together with vertical accelerations at the FP, heave and pitch motions. The 2-node frequency and the structrual damping

coefficients of the ship model floating in still water were also measured. The heave and pitch motions were measured by a 4-component motion measuring device. A servo needle type waveheight meter was firmly attached to the towing carriage with the probe positioned approximately 4.5m in front of the model's centre of gravity. Vertical accelerations were measured by an accelerometer installed on the deck at the centreplane of Station 20. The bending moments were measured through strain gauges fixed on the starboard side-deck plate at longitudinal stations. The relation between the vertical bending moment and the value of strain was derived by a static calibration method assuming that the creepage of the material is small and can be neglected. The locations of these measurement points were:

M_1 near Station 15 (2.65m from AP);

M_2 at Station 12.5;

M_3 near Station 10 (1.85m from AP);

M_4 at Station 7.5;

M_5 near Station 5 (0.95m from AP).

Model test experiments were undertaken in the towing tank of CSSRC to produce a sufficient length of record during each run. The experimental conditions (regular waves) are listed in Table 3. A sampling frequency of 100 Hz was chosen for all the wave conditions to analyze the transient responses due to impacting loads. Figure 2 shows the measurement locations on the model and a typical model test setting.

Table 3 Experiment conditions

Fn = 0.275			Head sea
Case	Wave	Wave height(mm)	Wave length (λ /L_{pp})
1	regular	$2a_w$=L/50=72	0.6,0.7,0.8,0.9,1.0,1.1,1.2,1.3,1.5,2.0
2	regular	$2a_w$=L/40=90	0.5,0.6,0.7,0.8,0.9,1.0,1.1,1.2,1.3,1.4,1.5,2.0
3	regular	$2a_w$=L/30=120	0.6,0.7,0.8,0.9,1.0,1.1,1.2,1.3,1.4,1.5,1.8,2.0
4	regular	$2a_w$=L/20=180	1.0,1.1,1.2,1.3,1.4,1.5,1.6,1.7,1.8,1.9,2.0,2.2

To distinguish any asymmetry characteristics in the vertical bending moment measured in the model in dynamic tests, zero levels were recorded when the model was at rest in still water. Therefore, the bending moment results are measured relative to static bending moment in still water, and include the vertical steady state bending moment component due to forward speed of the ship model at Froude number Fn=0.275. The steady state bending moments along the ship length were measured in the still water condition separately, and subtracted from the relevant dynamic test results in the afterward data analysis.

4 Test results and wavelet analysis

The 2-node flexible mode frequency (9.4 Hz) and the structural damping ratio (0.067) of the model floating in still water were measured by an impulsive loading technique (Chen et al 2001).

The non-dimensional expressions for the amplitude of vertical acceleration $\ddot{Z}_T$, pitch θ, heave Z and the vertical bending moment M are respectively given as:

$$C_A = \frac{L\ddot{Z}_T}{ga},\ C_\theta = \frac{\theta}{ka},\ C_Z = \frac{Z}{a},\ C_M = \frac{M}{\rho g L^2 Ba}$$

where L denotes ship length (L_{pp}), B, ship breadth, ρ, fluid density, g, acceleration of gravity, k, wave number.

A power of 2 sample points was chosen for the wavelet analysis, and 2048 (i.e. 2^n, n=11) consequent points were selected from each record. This represents a duration of over 20 seconds for each wave condition.

For the mathematical model described in section 2 and, in particular equation (10) is deemed successful, then it is expected that a wavelet reproduction form of equation (10) approximates closely to the original data without evident error at the ends of the truncated data set. Figure 3 illustrates comparisons of the results near the end of the truncated data (t=20.48 second) between a mid-ship vertical bending moment measured records and reproduced data by the wavelet families defined by different vanishing moment N and different data extension

methods (i.e. mirror, cubic spline). These comparisons demonstrate that there is no evident edge effect due to the extension of the dataset using mirror or cubic spline extension method, but the numerical approximation adopting a Daubechies wavelet family with vanishing moment N= 2 generally overestimates peak and trough regions. As clearly shown this weakness is overcome by employing a Daubechies wavelet family with vanishing moment N= 10, in which the relative error is less than 10^{-3}.

For the wavelet transform expressed in equation (10), to reproduce the test data a summation of all components at different frequency levels is required. In the present study a set of 2048 sampling points is assumed and performed, the total number of levels is 12 (i.e. n+1, from Level –1 to Level 10). For example, for a midship bending moment record at wave condition λ/L=1.2, 2a/L=1/20, and the wave encounter period is 1.02 (s), Figure 4 shows the time histories of bending moment at each of the 12 frequency levels. It illustrates the dominant components of the responses, the time-variation behaviour of each component, and each level component magnitude with time depending on frequency level (-1 to 10) characteristics. The variations observed at lower levels (i.e. –1 to +3) indicate a slower vibration behaviour. For example, the value at Level –1 describes the static component difference between sagging and hogging vertical bending moment, whilst components at Level 6 and Level 7 are dominated by the first harmonic and the second harmonic wave induced responses. The lower level frequency components exhibit steady variation with respect to time. However, for the higher level components, especially at Levels 8 and 9, an impulsive response behaviour is observed correlating with the impulsive excited interval of the encounter wave period. To examine in detail the frequency properties of each level component, Figure 5 illustrates a discrete cosine Fourier transform of both the original signal and the derived wavelet component at each frequency level of the summation of several wavelet components. For the vessel travelling in severe regular head waves, a typical response in the frequency domain of the mid-ship vertical bending moment is derived from the Fourier transform of the original data. It shows the dominant first harmonic component and higher harmonic components of not negligible values, especially responses relating to the second harmonic and 2-node natural frequency harmonic contributions. It is clear that the summation of components at Level 5 and Level 6 provides the main contribution to the whole response within the frequency region (0.5-1.5 Hz), whilst components at Levels 7, 8 and 9 contribute to the response in the frequency ranges (1.0-3.5Hz), (2.5-7.5Hz) and above 4.5Hz respectively. Frequency overlap of responses between adjacent levels exists, and therefore synthesis of several level components may be necessary to derive results for further analysis.

4.1 Rigid body motion responses

The original non-dimensional pitch and vertical acceleration records and their low and high frequency decomposition by the wavelet method are shown in Figure 6 for 2a/L=1/30 and λ/L=1.2. In this analysis, high frequency contributions are formed at frequency Level 9 and upward. From the original recorded data, unusual high frequency oscillations are observed in the pitch motion response, which appear after the pitch response reaches the trough value within each wave period. The maximum amplitude of these oscillations exceeds one third of the average amplitude of the total response. This problem appears in the pitch motion response records in nearly half of the wave conditions.

To investigate whether these high frequency oscillations are realistic components of rigid body motion responses, measured vertical accelerations at the bow are used for comparison. The pitch motion contributes to the vertical acceleration response at the bow, and therefore, a large-scale, higher frequency oscillation of pitch motion, if it is real, should be observed by a similar or even more severe oscillation at the same instant in the acceleration response. However, the phenomenon is not observed in the acceleration test result shown in Figure 6. To check the frequency characteristics of the pitch and bow vertical acceleration responses, Figure 7 shows the cosine Fourier transformation of the vertical acceleration at the bow as well as the low and high components of pitch motion. Note that, the results of the Fourier transform of the higher level components of pitch are shifted downwards by 0.1 to ensure a clearer picture. The vertical acceleration is dominated by the first wave harmonic response together with the second harmonic and 2-node flexible frequency (8-9 Hz) responses. The peak at 18 Hz in the FFT transform is the local deck vibration response, on which the accelerometer is installed. From these FFT transform results, the lower frequency level components of pitch response are principally formed from the first and second wave harmonic responses. The Fourier transform of the higher frequency level components cover evenly 4.5 to 25 Hz. A comparison between pitch and acceleration (i.e. time history and frequency transform results) show no evident relationship between the high frequency oscillation in the pitch record and the global impulsive responses in the vertical acceleration.

Similarly, a high frequency oscillation phenomenon occurs in the measured heave response, shown in Figure 8 for 2a/L=1/30 and λ/L=2.0. In this wave condition, the oscillations start when ship falls from its zenith locations. Again, there is no obvious connection between these heave high frequency oscillations and vertical

acceleration responses at the bow. It is also found that the occurrence of the unusual high frequency oscillations in pitch and heave records is not always observed for the same wave conditions. As an example, in the wave condition mentioned in Figure 6, no high frequency oscillation is observed in the heave motion record whereas occurrences are found in pitch motion records.

These findings confirm that the unusual high frequency oscillations in pitch and heave measured data are caused by local ship hull impulsive vibrations, and can be removed using the wavelet analysis method by artificially setting the coefficients to be zero at high frequency levels in equation (10). That is, frequency levels less than 9 are only included and the resultant peak and trough values of heave and pitch excited at different wave conditions are shown in Figure 9. Components of frequency at Level 9 or at higher levels represent responses exhibiting frequencies higher than 4.5Hz. Therefore the mean shift and first three harmonic responses of rigid body motions are at least covered in wavelet treated data for $\lambda/L>0.5$. For $\lambda/L=0.5$, in which the encounter frequency equals 1.8Hz, components up to the second harmonic are included. Analysis of all data shows that in wave states ($\lambda/L<1.1$ or $\lambda/L>1.4$), the non-dimensional rigid body motion responses behave in a reasonably linear manner. However, in the wavelength region, $1.1\leq\lambda/L\leq1.4$, green water on the deck was observed during the model tests, which causes reduction of peak values of the heave motion. The flare at the bow supplies additional buoyancy force and flare impact force during large motion excursions, reduce pitch peak values in these wave conditions. If the average of the peak and trough amplitude is defined as the response amplitude, it is observed that these values of both heave and pitch motions reduce evidently, coinciding with the phenomena reported by Fonseca and Soares (2004) for a S175 model. With the exception of the evident discrepancy between the peak and trough values of rigid body motions in experimental test condition Case 4 (2a/L=1/20) of Table 3, only slight differences are found for the other wave height conditions examined.

4.2 Vertical bending moments

Non-linear ship wave loads, such as vertical bending moment, are generally considered caused by large-amplitude non-linear waves, the variable geometry of the ship's hull as it plunges in and out of waves, as well as slamming, wave breaking and green water on deck (ISSC, 2000). The sagging and hogging bending moment responses reflect these non-linear characteristics. Data analysis of the mean shift and higher order harmonic components in the frequency domain provide an alternative way of representing sagging-hogging responses (Watanabe et al, 1989; Fonseca and Soares 2004; Chen et al, 2001). However, a time-history related information, such as the start of slamming, green water impact, decay behaviour of the impulsive structural responses associated with harmonics of frequency near the 2-node natural frequency of ship, are not easily derived. In such cases, a wavelet analysis is able to supply much information and demonstrates one of the benefits of this approach.

A conventional FFT analysis of bending moment measured in a flexible model test shows that the first harmonic and 2-node flexible natural frequency components are nearly of the same order in magnitude when the model travels in severe waves. The recorded second and third harmonic components are one or two orders smaller (Chen et al, 2001). Taking these findings into account, the measured vertical bending moment results are divided into a lower frequency level component (<Level 8) and a higher frequency level component in the wavelet method. The lower frequency component includes the mean shift, the first and second harmonic responses, whereas the higher frequency level component contains the higher harmonic responses, especially responses near the 2-node flexible natural frequency. Figure 10 shows a typical division in time domain of the original vertical bending moment sample recorded over a time into lower (<Level 8) and higher frequency (≥Level 8) components.

By adopting a peak and trough counting method, average sagging and hogging response amplitudes over a period of 20.48 second are obtained from the original bending moment measured data and lower and higher wavelet components data. Figure 11 shows the results for the amid-ship vertical bending moment in these three data cases allowing investigation of the asymmetry characteristics observed in the measured data. Compared to the rigid motion responses, the sagging and hogging asymmetry of the total measured bending is more evident for all the wave cases moments as shown in Figure 11 (a), especially in the wavelength region of λ/L=1.0-1.5. Figure 11(c) shows that the higher level frequency responses are almost sagging-hogging symmetric. Hence, Figure 11 (a) and (b) demonstrate the similar asymmetry behaviour and values at each corresponding wave condition are closely in agreement except in the wave height Case 4 (2a/L=1/20) and wavelength region λ/L=1.0-1.5. Therefore asymmetry is essentially caused by the mean shift value, the first and second harmonic response. It is also interesting to notice that the sagging and hogging values derived from the original measured data are not simply the summation of these corresponding values obtained by the lower and higher frequency level components. In general the summation of these two hogging values is larger than the one obtained from the original measured data, and an opposite tendency is found for the sagging cases. Table 4 explains this phenomenon in detail and an explanation can be found from Figure 10. In particular is the impulsive vibration

starts when the hull girder is passing from hogging to sagging condition, and reaches the maximum value at the moment when sagging peak appears. In this worst severe wave condition during the test, the maximum amplitude of the higher level frequency component is even larger than the corresponding value of the lower level frequency component which is dominated by the mean shift and the first harmonic responses. The main high frequency of vertical bending moment after impact is about 9.0 Hz, close to the 2-node wetted natural frequency of the model ship. After the appearance of a peak value, the high frequency level components of response exhibit a conventional damped free vibration behaviour. At the moment the hogging peak appears in the total response, the amplitude of the higher frequency level component reduces to about a quarter of the maximum value. The contribution of the higher frequency level components on the sagging and hogging values of the total bending moment is not negligible in wavelength region of λ/L=1.0-1.5, makes both sagging and hogging values and the asymmetry between them to increase.

Table 4 Sagging and hogging values of mid-ship vertical bending moments C_{M3} *100 (Case 3)

λ/L	Measured data		Lower levels		Higher levels	
	Hogging	Sagging	Hogging	Sagging	Hogging	Sagging
0.6	1.167	-1.617	1.013	-1.427	0.3043	-0.3074
0.7	1.290	-1.648	1.067	-1.478	0.3043	-0.3360
0.8	1.397	-2.240	1.324	-1.852	0.3181	-0.3360
0.9	1.305	-2.485	1.045	-1.931	0.3708	-0.3789
1.0	1.267	-3.094	0.961	-2.282	0.6127	-0.6155
1.1	1.143	-3.735	0.966	-2.827	0.5589	-0.6775
1.2	1.816	-3.875	1.315	-2.847	0.4406	-0.4578
1.3	1.357	-3.128	1.235	-2.667	0.7580	-0.5891
1.4	1.457	-2.785	1.174	-2.426	0.4591	-0.6576
1.5	1.278	-2.444	1.131	-2.310	0.2818	-0.4276
1.8	0.800	-1.530	0.707	-1.411	0.2540	-0.3169
2.0	0.684	-1.079	0.607	-0.992	0.0703	-0.1114

In the rigid body response analysis, normally the unusual high impulsive oscillation in the pitch motion record was shown to be an unrealistic response. However there remains the possibility that it could indicate the occurrence of flare impact in severe seas. Further studies were undertaken to assess the relative vertical motions between the incoming wave and a point located on the mean waterline surface at Station 19, and the start and cause of impulsive high frequency vibrations. A waveheight meter was installed 4.5m ahead of the centre of gravity of the ship model. The shift in time between the measured incoming wave reaching the chosen point near the bow is numerically calculated from the wave phase velocity, ship's forward speed and the distance between these two locations. Steady and unsteady disturbed wave profiles and surge motion are not included in the relative vertical motion calculation, therefore these derived data can only be used qualitatively to investigate the green water problem.

Figure 12 shows the wavelet analysis division of high (≥Level 8) and low (<Level 8) frequency level components of the mid-ship vertical bending moment, the high level component of measured pitch motion data, the low frequency component of the relative vertical rigid body motion at Station 19 (shown as 'zw') and the incoming wave passing through this location (shown as 'awave'). The results for incident waves with wavelengths from λ/L=0.7 to 2.0 and wave height (2a/L=1/30) are presented. It is observed in Figure 12 that the impulse response components of the vertical bending moment generally occur twice within one wave period. One commences when the bow starts moving downwards, accompanied by a high frequency oscillation signal in the measured pitch record, whilst the other begins just after the wave peak passes through the bow area. When these two events nearly coincide, as shown at wavelength λ/L=1.5, a single impulse excitation and a 2-node natural frequency free vibration response are evident. In long waves, i.e. λ/L=2.0, the high frequency component in the bending moment response is comparatively small in comparison with the low frequency component consisting of the mean shift and first harmonic responses. However, with decreasing wavelength,

especially for an incident wave of approximately one ship length, the maximum amplitudes of the high frequency whipping response are of the same order of magnitude to the corresponding values of the low frequency components. For example, for $\lambda/L=1.0$, the ratio of these values is approximately 0.8, whereas for $\lambda/L=1.2$, this ratio reduces to 0.7 approximately. It is interesting to note that for $\lambda/L=1.0$-1.5, impulsive impacts occur about 30 degrees ahead of the wave-induced sagging peak of the bending moment, and decay to nearly one third of the maximum amplitude in the hog state. These dynamic variations, together with a negative mean shift in the bending moment mainly caused by the changing geometric properties of the instantaneous wetted hull surface, make sagging values of the total bending moment two times larger than hogging values.

Of course, it is clear that the extent of the high frequency response contribution on the total bending moment also depends on the incident wave heights. Figure 13 shows the same kinds of results for other three wave height cases when the wavelength is $\lambda/L=1.2$. Once again the ratios between the maximum amplitudes of the high frequency whipping response and that of the lower frequency components for those three cases are 0.4, 0.6, 1.7. In the most severe wave case, i.e. $2a/L=1/20$, the maximum value of the whipping response amplitude is even larger than the corresponding value of the lower frequency component and starts at the sagging peak of the bending moment. The second impulsive responses following flare impact are detected in Case 4, nearly half a wave encounter period delayed. Referring to the relative vertical motion at the bow and the lower frequency component of the bending moment, these second impulsive responses of mid-ship vertical bending moment are identified as the response of green water impact. The visual record also confirms the occurrences of severe green water on the deck during the model test at this severe wave condition. If we use the variation between the maximum impulsive response amplitude and the higher frequency amplitude one period ahead as an indicator to measure the scale of the impacting forces in Figure 13 (c), it can be found that this factor for flare impact is about 0.032, whilst 0.0074 only for green water impact. Even though green water impact was considered to be one of the main sources for the damage on bow and deck structures of ships such as FPSO (Stansberg and Karlsen, 2001), from the present results it demonstrates that flare impact is possibly a more important event to hull girder strength in severe seas.

Fig 14 illustrates bending moments at different longitudinal locations along the model. In the most severe wave condition, i.e. $2a/L=1/20$ and $\lambda/L=1.2$, the maximum impulsive sag response value, caused by flare impact, is larger than the corresponding low frequency component value and occurs approximately 30 degrees ahead of the wave-induced sagging peak of the bending moment. The second impulsive response is detected nearly half a wave encounter period afterwards. Relative vertical bow motion and a low frequency component in the bending moment record show that the second impulsive response in the mid-ship vertical bending moment is identified as caused by green water impact. The visual experimental records confirm the occurrence of severe green water on the deck during the tests at this severe wave condition. At the measuring point close to the bow, i.e. M_1, the flare impact response and green water impact are even more evident. The variation between the maximum impulse response amplitude (sagging) and the high frequency amplitude (hogging) occurring a half period ahead, are adopted as indicators to measure the scale of the impact forces. It is found in Figure 13 (c) that for measurement M_3 (amidships), the flare impact value is approximately 0.032, the green water impact value is 0.0074. By comparison, the amplitudes of the wave-induced sag and hog bending moments are 0.036 and 0.016 respectively. At measuring positions No.1, 2, and 4 these values are (0.018, 0.0056), (0.030, 0.0076), and (0.030, 0.0038) respectively. Green water effects have little influence on measured data at position No.5 (aft of amidships), but the flare impact value is approximately 0.014. Because vertical bending moments are measured by strain gauges glued to the deck, local deformations at the fixing point may magnify the contribution of green water impact on the measured total vertical bending moment. That is, the impulse exciting high frequency responses of the hull girder caused by the green water are possibly smaller than the measured value.

5 Conclusions

A wavelet analysis technique is developed to investigate non-linear wave-induced loads and motion responses using measurements on a S175 flexible model travelling in severe waves.

Rigid body motions nearly obey a linear relationship, except for results analyzed in wavelength region $1.1\leq\lambda/L\leq1.4$. However, asymmetry between peak and trough values of the responses and variations in the results measured for different wave heights are confirmed. The unrealistic high frequency oscillations in pitch and heave signals are found caused by the high frequency local deformation at the base of the motion measurement system and are removed systematically by the wavelet method.

The low and high frequency time history components of the vertical bending moment were deduced through the wavelet analysis technique. The low frequency component contains steady responses, i.e. the mean shift and first harmonic responses, whereas the high frequency component represents the transient responses, consisting of higher harmonics relating to the 2-node wetted natural frequency of the flexible ship.

These high frequency responses behave as a freely decaying vibration excited by transient impact loads. Dynamic characteristics, i.e. start of impact, maximum value of whipping amplitude etc., are deduced from the wavelet-derived data. The phase lag relation between impact occurrence, sagging and hogging peak values are easily observed. In general, flare impact increases the sagging peak value, whereas green water impact magnifies the hogging peak value.

Reference:

Chen RZ, Du SX, Wu YS, Lin JR, Hu JJ and Yue YL (2001). "Experiment on extreme wave loads of a flexible ship model", PRADS'2001, September 2001, Shanghai, China, pp.871-878.

Ciappi E, Dessi D and Mariani R (2003). "Slamming and whipping response analysis of a fast monohull via a segmented model tests", Hydroelasticity in Marine Technology, 2003, Oxford, UK, pp.143-153.

Cusano G, Monti S and Velasco A(2003). "Full scale and test investigation of slamming effects on fast mono-hull vessels", Proceedings of the third international conference on hydroelasticity in marine technology, Oxford, UK, September 2003, pp.164-173.

Daubechies I (1992), *Ten Lectures on Wavelets*, the Society for Industrial and Applied Mathematics, Philadelphia, PA

Faltinsen OM, Greco M and Landrini M (2002). "Green water loading on a FPSO", Journal of Offshore and Arctic Engineering, Vol. 124, pp.97-103.

Fonseca N and Soares C.G (2004). "Experimental investigation of the nonlinear effects on the vertical motions and loads of a containership in regular waves", Journal of Ship Research, Vol.48, No.2, pp.118-147.

ISSC (2000). Committee VI.1 report Extreme Hull Girder Loading, Proceedings of the 14th ISSC, Edited by H. Ohtsubo and Y.Sumi, Nagasaki, Japan.

Jensen JJ and Mansour AE (2003). "Estimation of the effect of green water and bow flare slamming on the wave-induced vertical bending moment using closed-form expressions", Hydroelasticity in Marine Technology, 2003, Oxford, UK, pp.155-161.

Kwon SH, Lee HS, Park JS, Ha MK and Kim YJ (2001). "Analysis of ringing by continuous wavelet transform", PRADS'2001, September 2001, Shanghai, China, pp.587-592.

Li QH, Du SX, Lin JR, Qiu Q, Wu YS (1996). " Hydroelastic theories and experiment of a elastic ship model", Advances in Hydrodynamics, Series A, Vol.11, No.2.

Lin J, Qiu Q, Li Q, Wu Y (1991). "Experiment of an elastic ship model and the theoretical predictions of its hydroelastic behaviour", Proc. of 1st Intl. VLFS, Honolulu, Hawaii, USA, pp.262-275

Newland DE (1993). *An Introduction to Random Vibrations, Spectral & Wavelet Analysis*, Third edition, Longman Scientific & Technical.

Nievergelt Y (1999). *Wavelet Made Easy*, Birkhauser, Boston

Patsias S, Staszewski WJ and Tomlinson GR (2002a). "Image sequences and wavelets for vibration analysis Part 1: edge detection and extracting of natural frequencies", Proc Instn Mech Engrs Vol 216 Part C, pp. 885-900.

Patsias S, Staszewski WJ and Tomlinson GR (2002b). "Image sequences and wavelets for vibration analysis Part 2: extraction of modal dampings and modal shapes", Proc Instn Mech Engrs Vol 216 Part C, pp. 901-912.

Percival DB and Walden AT (2000), *Wavelet Methods for Time Series Analysis*, Cambridge University Press.

Stansberg CT and Karlsen SI (2001). "Green water and water impact on FPSO in steep random waves", PRADS'2001, September 2001, Shanghai, China, pp.593-601.

Storhaug G, Vidic-Perunovic J, Rudinger F, Holtsmark G, Helmers JB and Gu XK(2003). "Spring/whipping response of a large ocean going vessel – A comparison between numerical simulations and full-scale measurements", Hydroelasticity in Marine Technology, 2003, Oxford, UK, pp.117-129.

Watanabe I, Keno M and Sawada H (1989). "Effects of bow flare shape on wave loads of a container ship", Journal of the Society of Naval Architects of Japan, Vol. 166, pp.259-266.

Wu YS, Chen RZ and Lin JR (2003). "Experimental technique of hydroelastic ship model", Hydroelasticity in Marine Technology, 2003, Oxford, UK, pp.131-142.

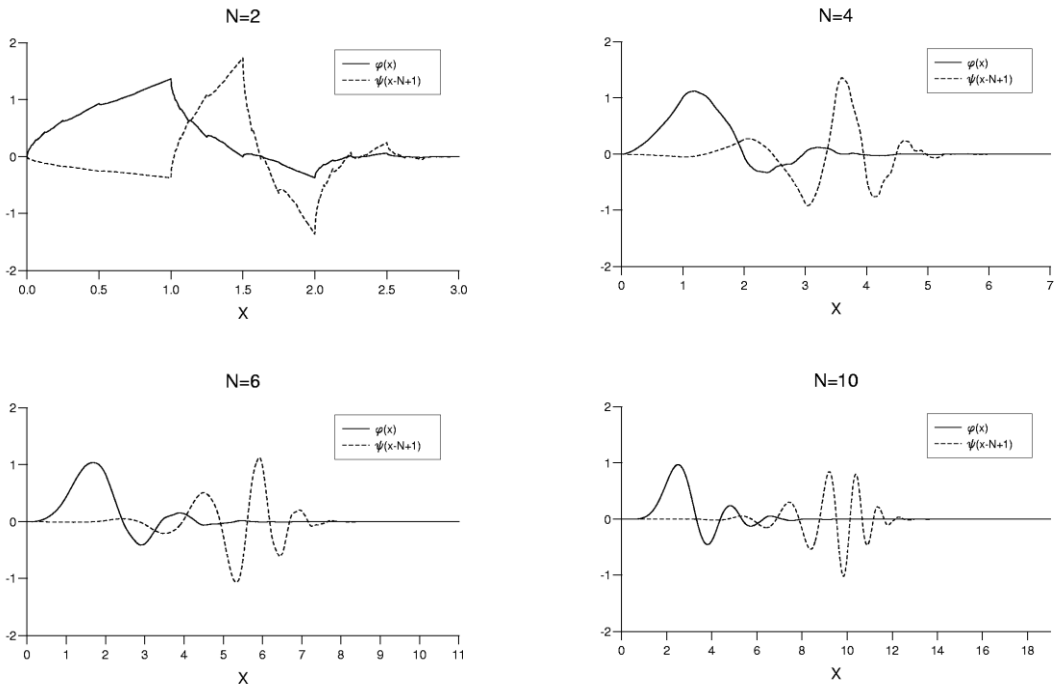

Figure 1 Scaling function and wavelet function bases for Daubechies wavelet family with vanishing numbers

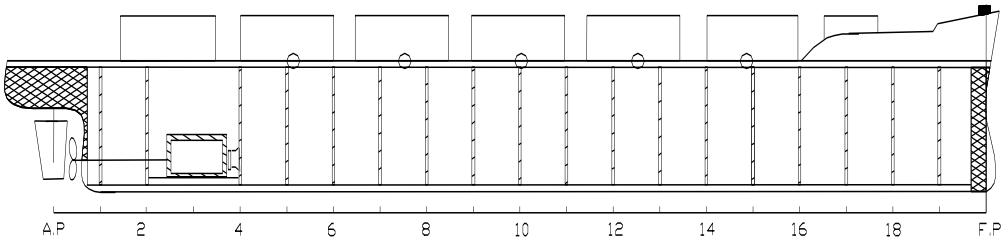

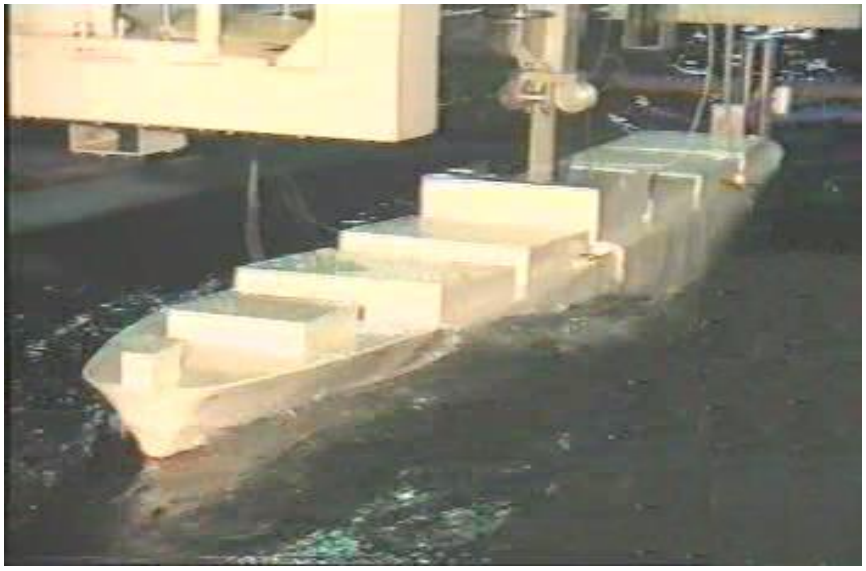

Figure 2 Flexible model of S175 container ship and measurement locations

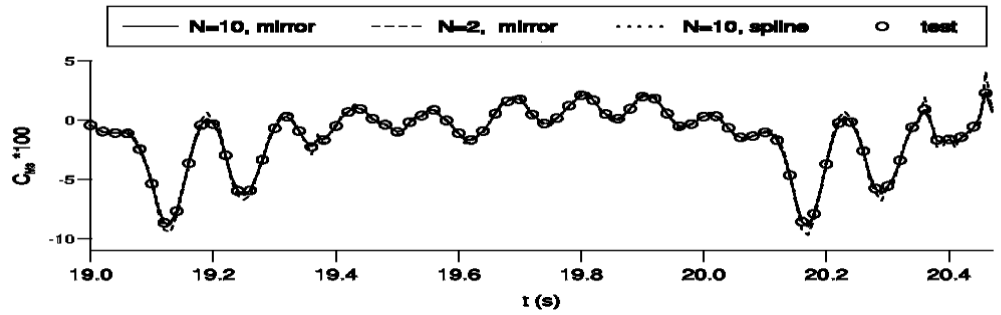
N=10, mirror
N=2, mirror
N=10, spline
test
5
0
-5
-10
19.0
19.2
19.4
19.6
19.8
20.0
20.2
20.4
t (s)

F es

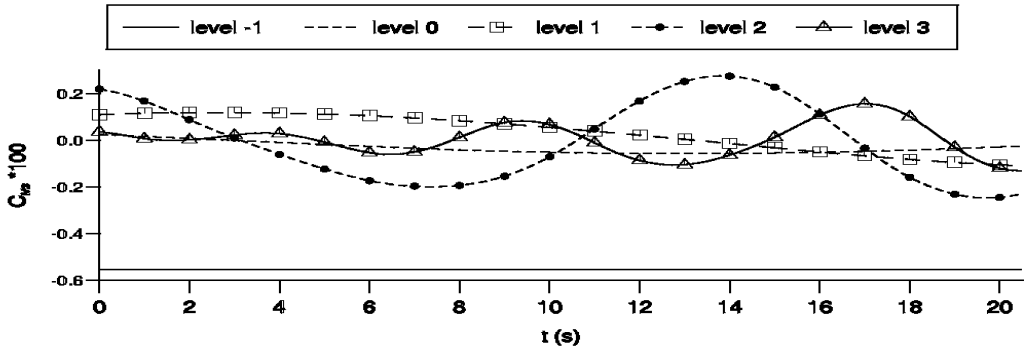
level -1
level 0
level 1
level 2
level 3
0.2
0.0
-0.2
-0.4
-0.6
0
2
4
6
8
10
12
14
16
18
20
t (s)

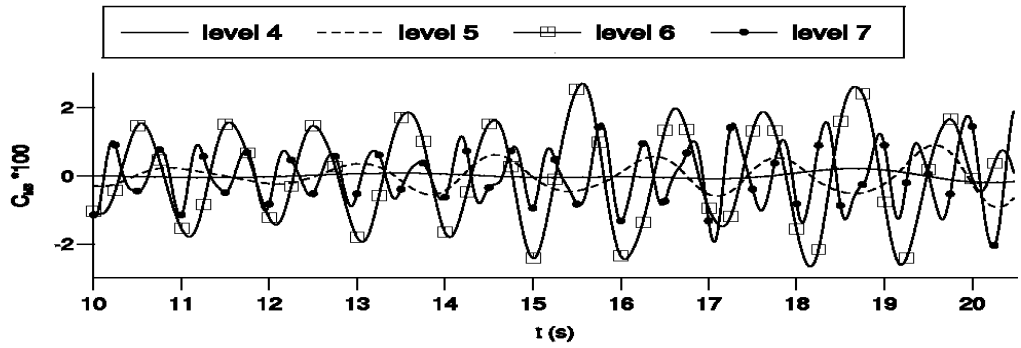
level 4
level 5
level 6
level 7
2
0
-2
10
11
12
13
14
15
16
17
18
19
20
t (s)

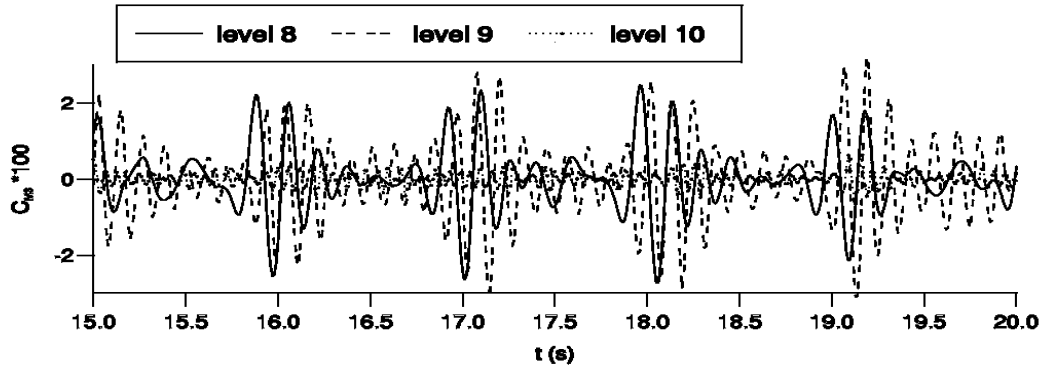
level 8
level 9
level 10
2
0
-2
15.0
15.5
16.0
16.5
17.0
17.5
18.0
18.5
19.0
19.5
20.0
t (s)

3

Figure 4 Decompositions of test data by wavelets (λ/L=1.2, 2a/L=1/20)

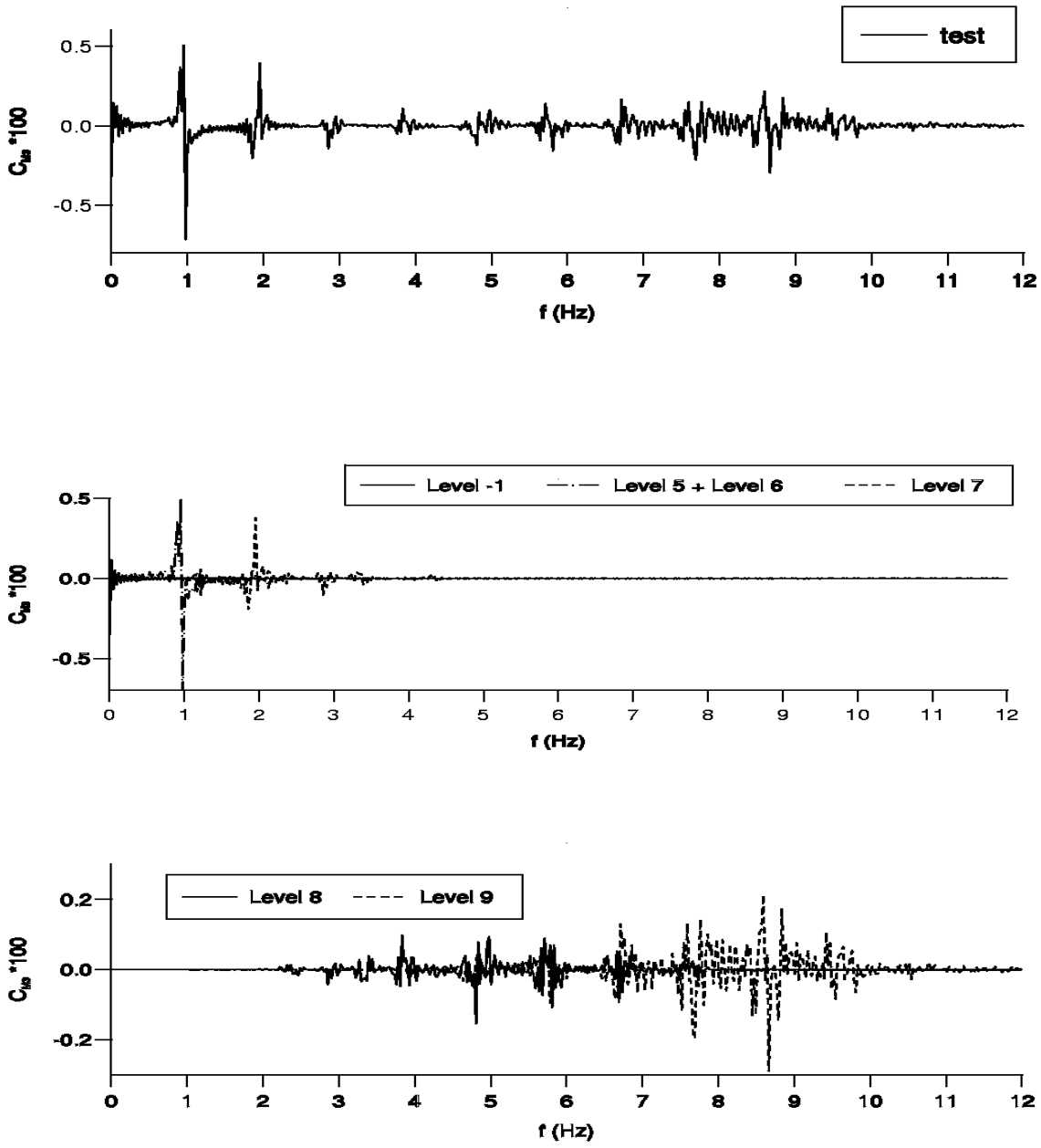

Fig

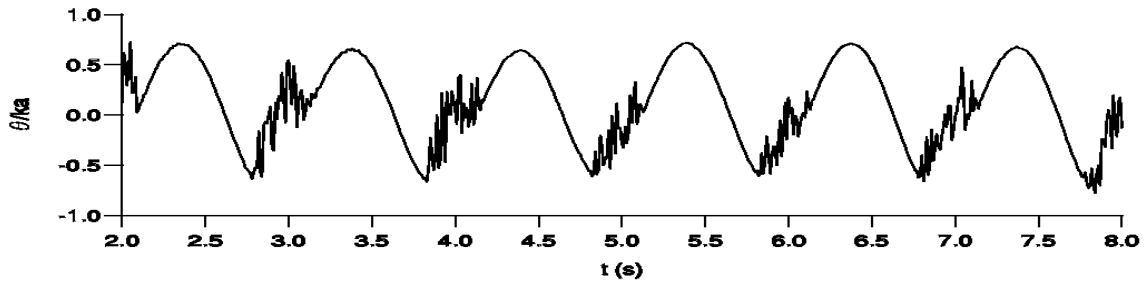
1.0
0.5
0.0
-0.5
-1.0
θ/kа
2.0 2.5 3.0 3.5 4.0 4.5 5.0 5.5 6.0 6.5 7.0 7.5 8.0
t (s)

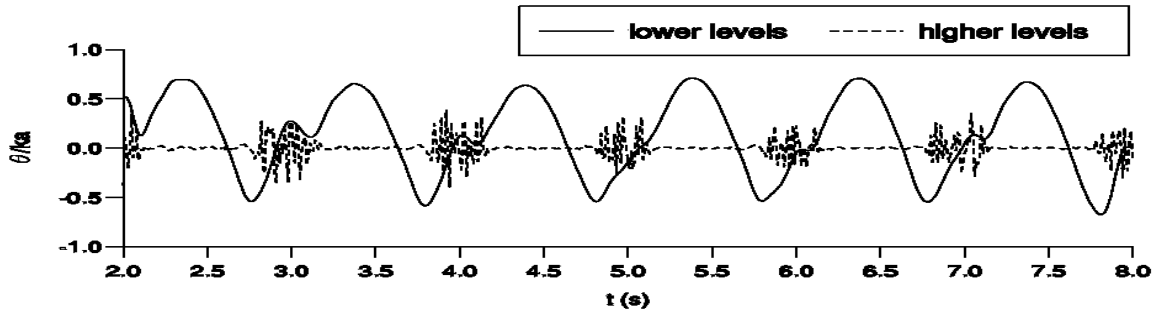
lower levels
higher levels
1.0
0.5
0.0
-0.5
-1.0
θ/kа
2.0 2.5 3.0 3.5 4.0 4.5 5.0 5.5 6.0 6.5 7.0 7.5 8.0
t (s)

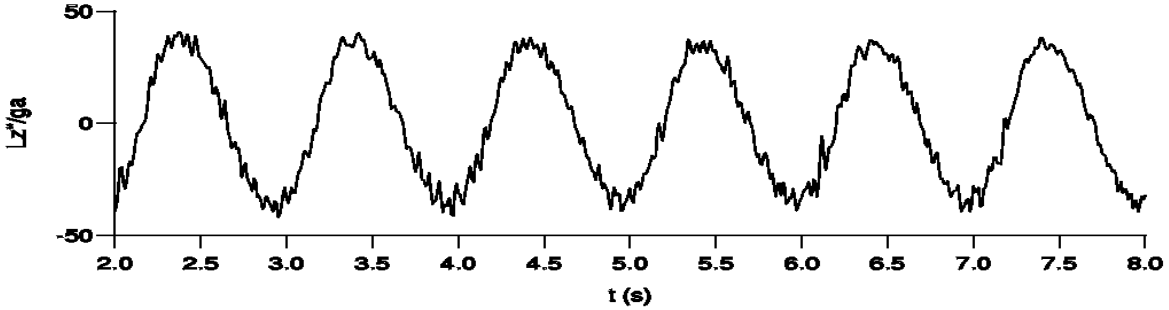
50
0
-50
Lx'/gа
2.0 2.5 3.0 3.5 4.0 4.5 5.0 5.5 6.0 6.5 7.0 7.5 8.0
t (s)

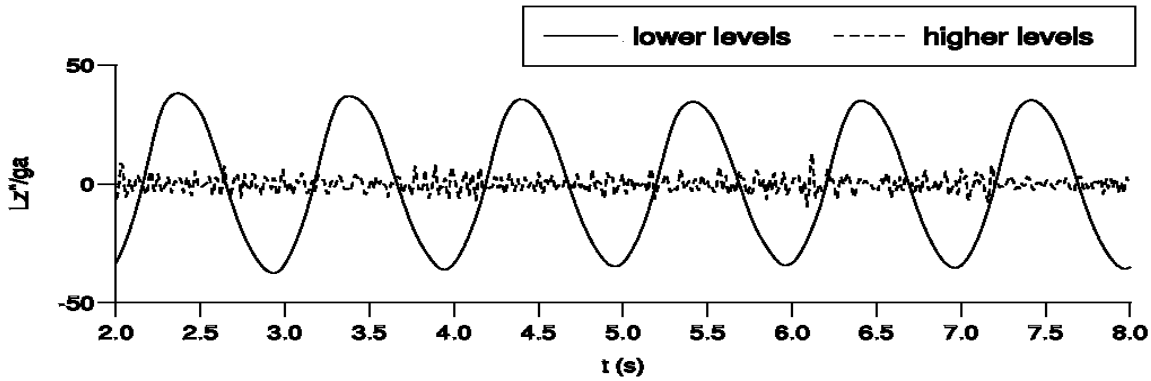
lower levels
higher levels
50
0
-50
Lx'/gа
2.0 2.5 3.0 3.5 4.0 4.5 5.0 5.5 6.0 6.5 7.0 7.5 8.0
t (s)

Figure 6 Decompositions of pitch and vertical acceleration at bow by wavelet analysis (λ/L=1.2, 2a/L=1/30)

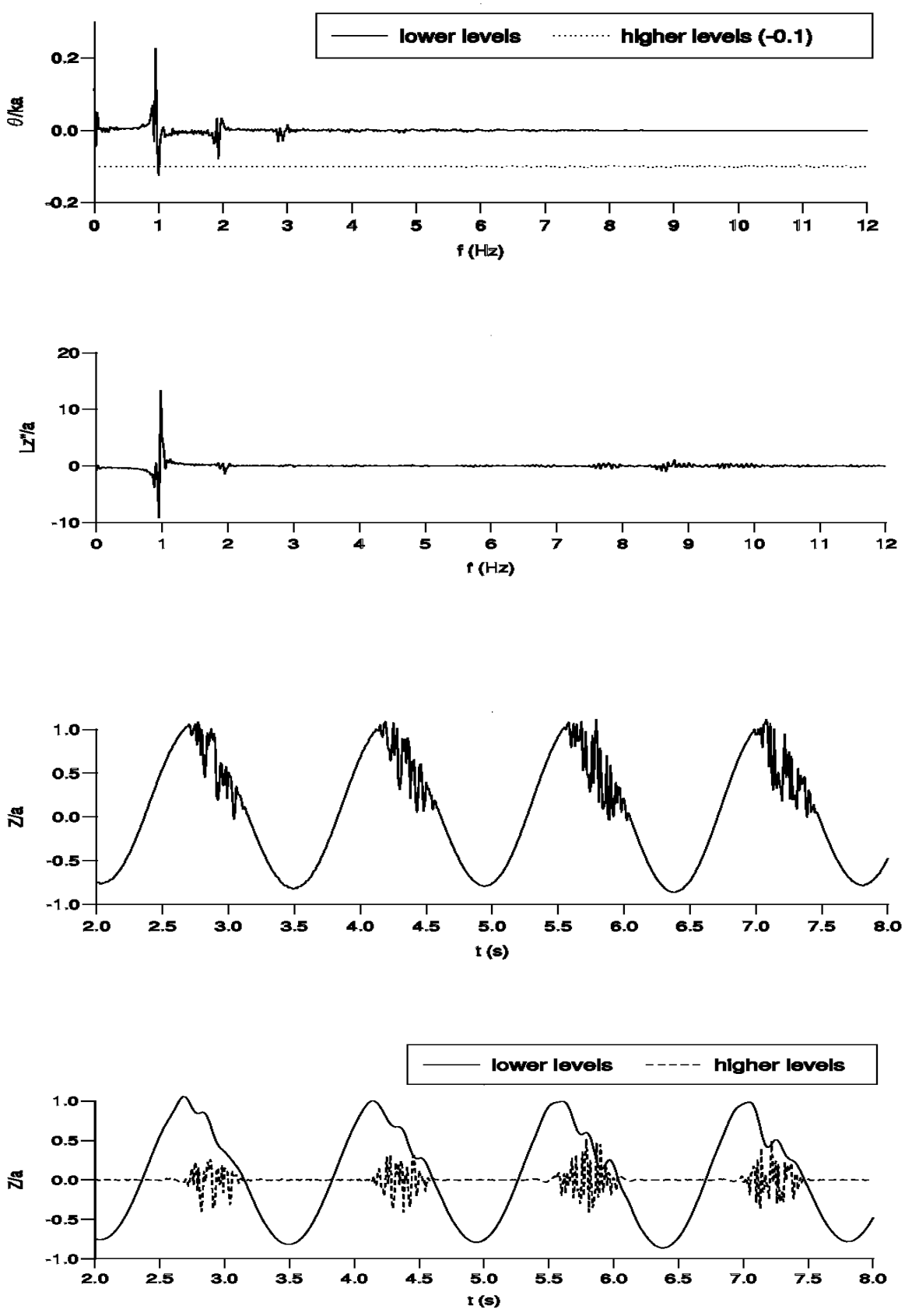

(b) Lower (<Level 8) and higher (≥Level 8) wavelet heave motion components

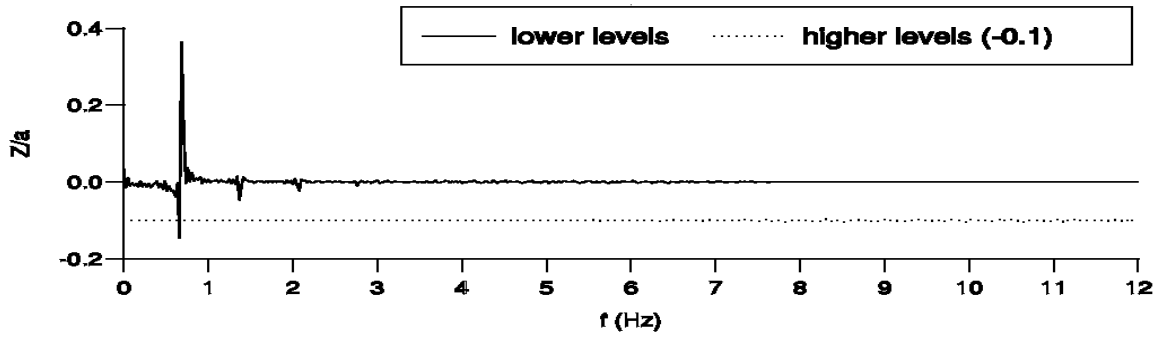

Fi

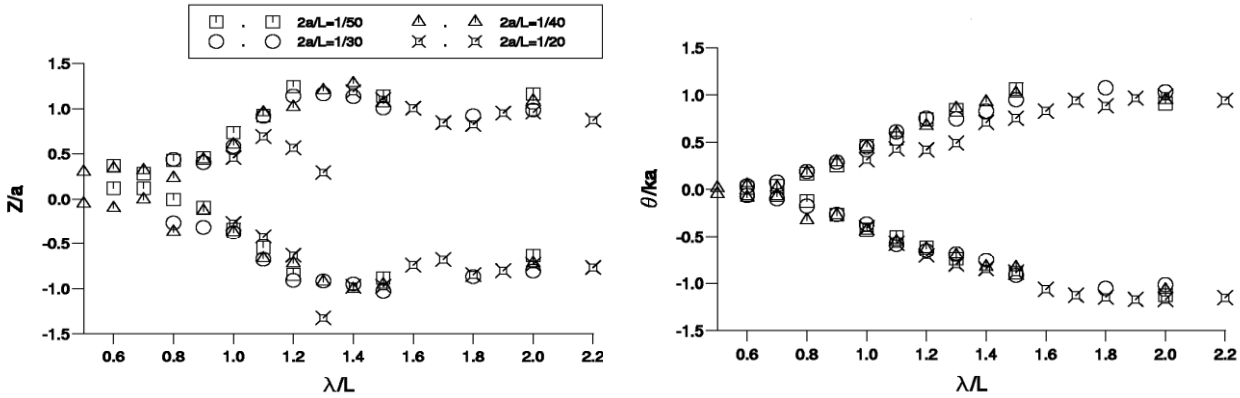

Figure 9 Peak and trough values of heave and pitch motions

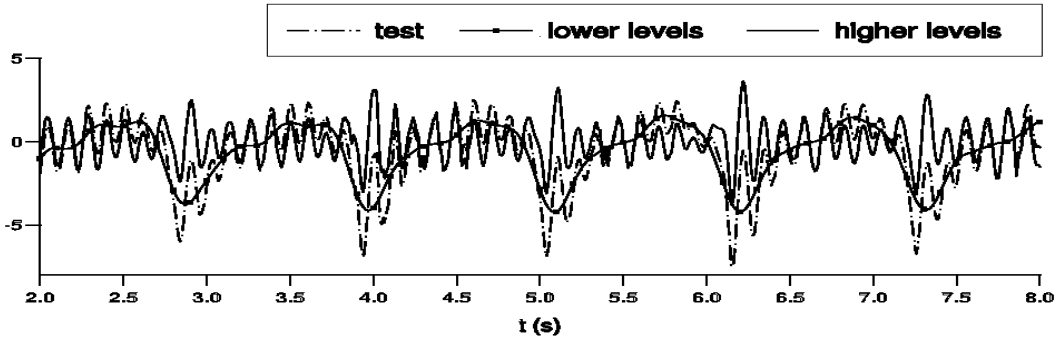

Fi

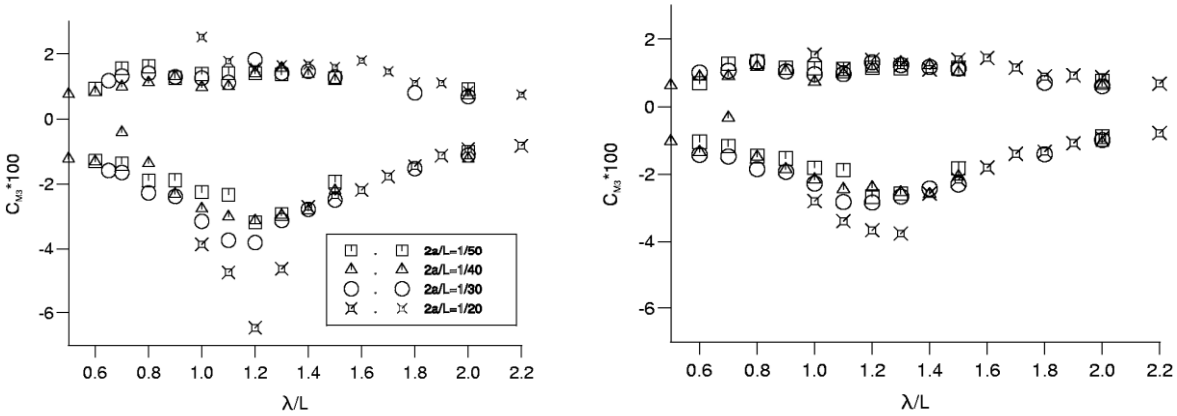

(a) Original measure data (b) Lower level frequency component

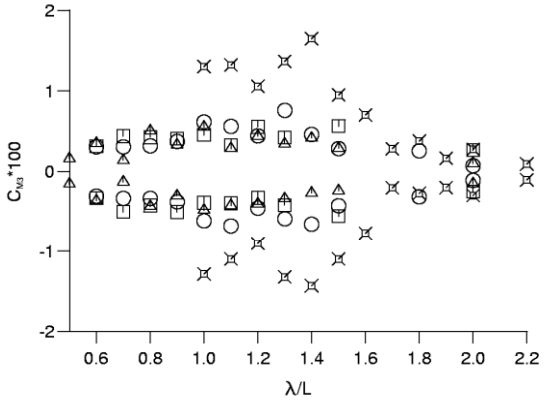

(c) Higher level frequency component

Figure 11 Sagging and hogging vertical bending moments at amidship

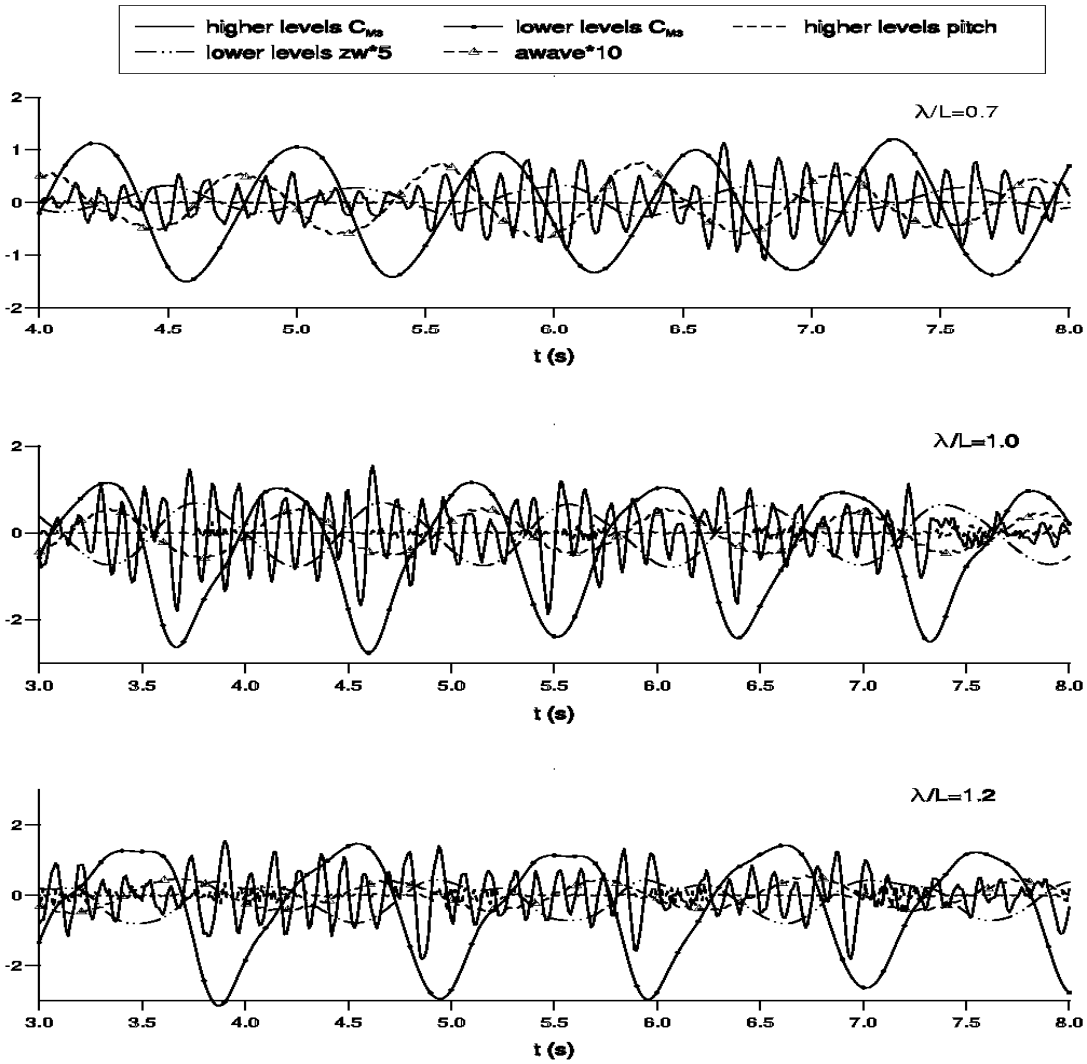

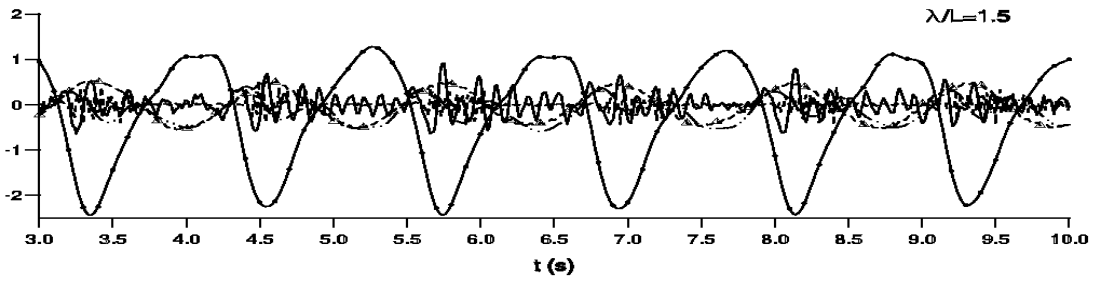
λ/L=1.5
t (s)

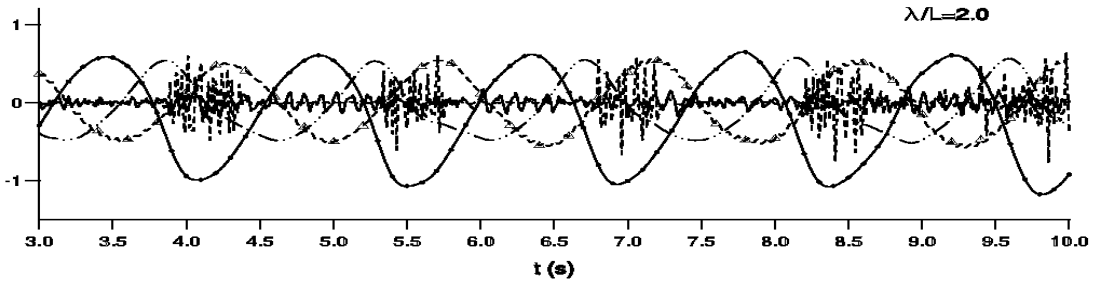
λ/L=2.0
t (s)

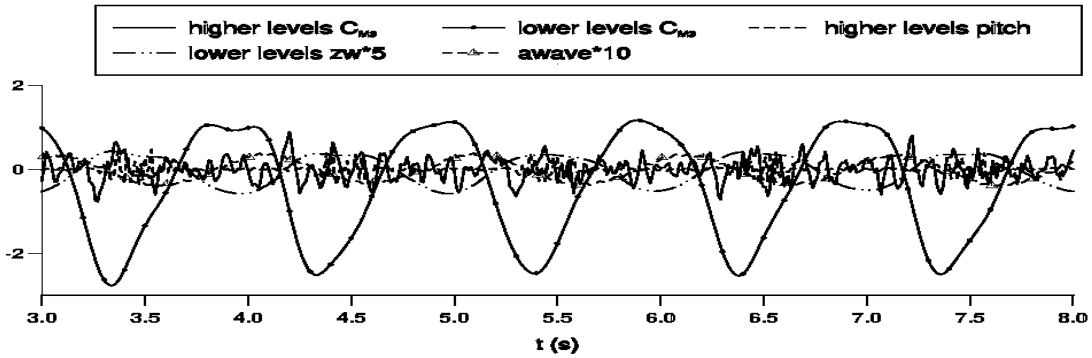
higher levels C_M3
lower levels C_M3
higher levels pitch
lower levels zw*5
awave*10
t (s)

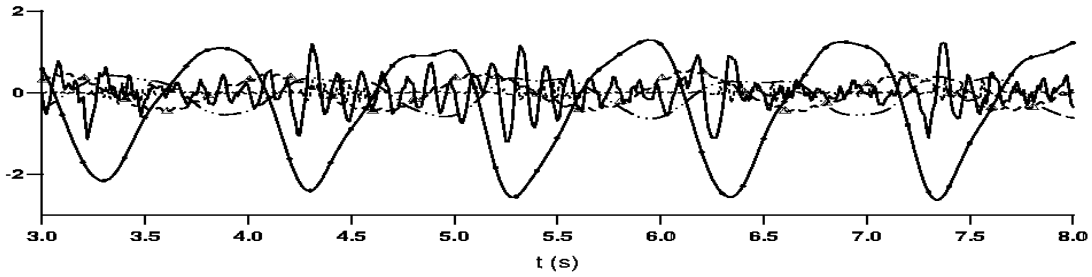
t (s)

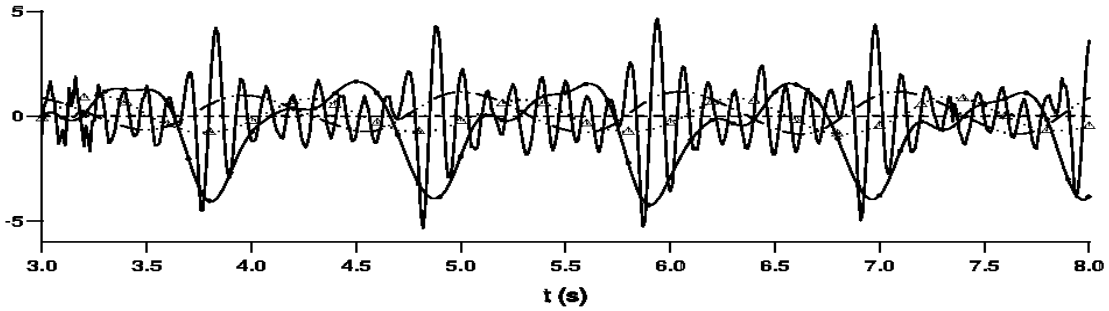
5
0
-5
3.0
3.5
4.0
4.5
5.0
5.5
6.0
6.5
7.0
7.5
8.0
t (s)

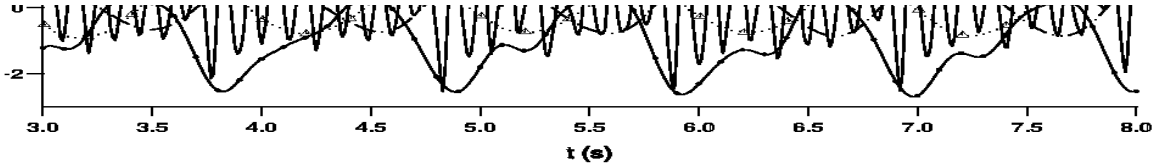
-2
3.0
3.5
4.0
4.5
5.0
5.5
6.0
6.5
7.0
7.5
8.0
t (s)

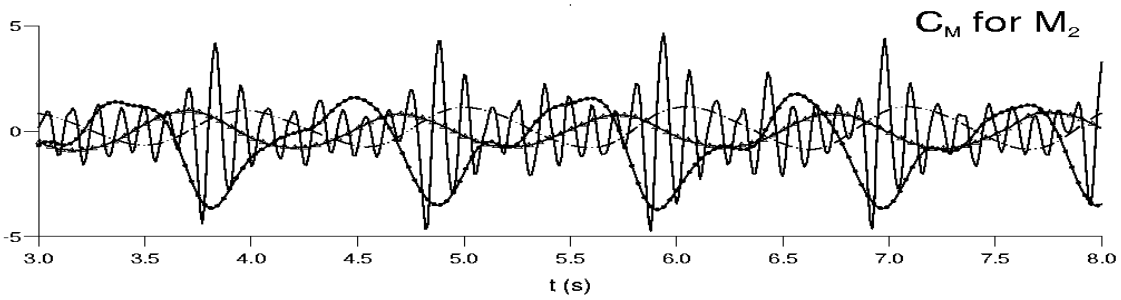
C_M for M_2
5
0
-5
3.0
3.5
4.0
4.5
5.0
5.5
6.0
6.5
7.0
7.5
8.0
t (s)

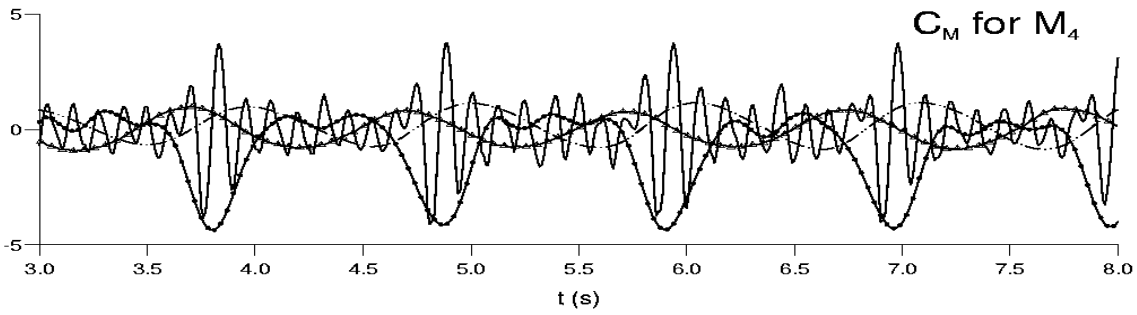
C_M for M_4
5
0
-5
3.0
3.5
4.0
4.5
5.0
5.5
6.0
6.5
7.0
7.5
8.0
t (s)

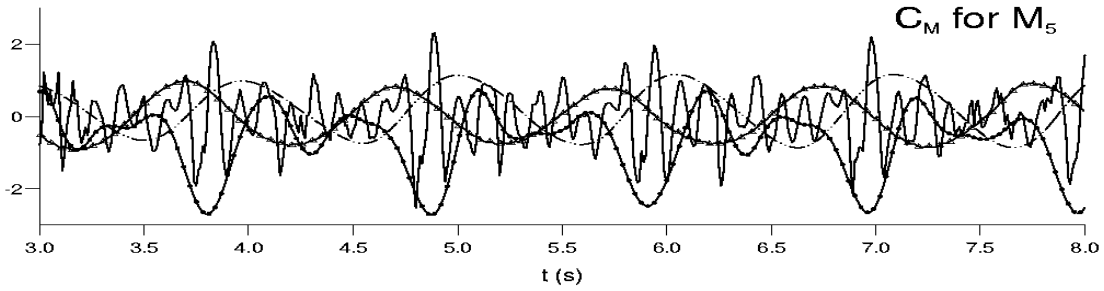

Figure